



Article

Artificial Synapses Based on an Optical/Electrical Biomemristor

Lu Wang *, Shutao Wei, Jiachu Xie, Yuehang Ju, Tianyu Yang and Dianzhong Wen

Heilongjiang Provincial Key Laboratory of Micronano Sensitive Devices and Systems, School of Electronic Engineering, Heilongjiang University, Harbin 150080, China

* Correspondence: wanglu@hlju.edu.cn; Tel.: +86-188-4502-5666

Abstract: As artificial synapse devices, memristors have attracted widespread attention in the field of neuromorphic computing. In this paper, Al/polymethyl methacrylate (PMMA)/egg albumen (EA)-graphene quantum dots (GQDs)/PMMA/indium tin oxide (ITO) electrically/optically tunable biomemristors were fabricated using the egg protein as a dielectric layer. The electrons in the GQDs were injected from the quantum dots into the dielectric layer or into the adjacent quantum dots under the excitation of light, and the EA-GQDs dielectric layer formed a pathway composed of GQDs for electronic transmission. The device successfully performed nine brain synaptic functions: excitatory postsynaptic current (EPSC), paired-pulse facilitation (PPF), short-term potentiation (STP), short-term depression (STD), the transition from short-term plasticity to long-term plasticity, spike-timing-dependent plasticity (STDP), spike-rate-dependent plasticity (SRDP), the process of learning, forgetting, and relearning, and Pavlov associative memory under UV light stimulation. The successful simulation of the synaptic behavior of this device provides the possibility for biomaterials to realize neuromorphic computing.

Keywords: physical transient; biological materials; graphene quantum dots; OR gate



Citation: Wang, L.; Wei, S.; Xie, J.; Ju, Y.; Yang, T.; Wen, D. Artificial Synapses Based on an Optical/Electrical Biomemristor. *Nanomaterials* **2023**, *13*, 3012. <https://doi.org/10.3390/nano13233012>

Academic Editor: George Z. Kyzas

Received: 7 September 2023

Revised: 21 October 2023

Accepted: 25 October 2023

Published: 24 November 2023



Copyright: © 2023 by the authors. Licensee MDPI, Basel, Switzerland. This article is an open access article distributed under the terms and conditions of the Creative Commons Attribution (CC BY) license (<https://creativecommons.org/licenses/by/4.0/>).

1. Introduction

Different from the traditional von Neumann computer architecture, neuromorphic computing, as a new type of computer system, has the advantages of a low power consumption, a high efficiency, and a high fault tolerance. Because it solves the problem of expensive data transfer between the processor and the memory, it has become a hot area worthy of in-depth study [1–5]. As an emerging nonvolatile device, the memristor changes its own resistance through the stimulation of the external voltage, similarly to a biological synapse, simulating the change in synaptic weight in a biological synapse. It is considered an ideal device for studying neuromorphic computing [6–8]. The low power consumption, scalability, high density, and nonvolatility of memristors facilitate the realization of synaptic behaviors in biological neurons [9–11], which are capable of performing, learning, memory, and other complex neural behaviors [12–15], making them a key element in neuromorphic computing research. Previous memristor research achieved a variety of synaptic behaviors, such as short-term plasticity, excitatory postsynaptic current (EPSC), paired-pulse facilitation (PPF), long-term plasticity (STP), spike-rate-dependent plasticity (SRDP), and pulse-time-dependent plasticity (STDP) [16–20].

In an effort to find suitable materials for fabricating artificial synapses, a wide variety of materials have come into the field of researchers, such as metal oxide materials [21], inorganic materials [22,23], chalcogenides [24], perovskites [25–29], and 2D materials [30,31]. Most of the materials reported in the literature are complex to prepare and incompatible with organisms [32–34], making them difficult to use due to a lack of environmentally friendly disposal methods and for posing potential threats to the environment. Therefore, to produce biocompatible devices at a low cost, new materials must meet these requirements, using readily available natural compounds. Organic materials are widely used in the preparation and research of resistive switching layers due to their low cost and nonpolluting

environment [35–37]. Memristors made of natural biomaterials are widely used in wearable, compatible, and environmentally friendly smart electronic devices; among these materials are lignin [38], pectin [39], chitosan [40], and anthocyanins [41], which have been used as the memristors' active layer of a device. In addition, protein materials are also widely used in artificial synapse devices because of their good biocompatibility, degradability, specificity, and ease of processing. By regulating the synthesis process of protein materials or modifying them after synthesis, their structure and properties can be adjusted. As a protein material, egg albumen has good degradability and biocompatibility and can be absorbed by the human body. Moreover, egg albumen is a protein material with variable electrical conductivity, which is similar to the neuroplasticity of biological synapses and can simulate the synaptic connections between biological neurons. Therefore, egg albumen has been used as an active or dielectric layer in fabricating high-performance resistive switching devices [36] and thin-film transistors [34]. However, in-depth research on biomaterial-related synaptic bionics and neuromorphic computing remains incomplete.

Biomemristors have been extensively studied recently. Yan et al. used EA as an active layer to prepare a flexible W/EA/ITO/PET device, which can shift from paired pulse facilitation to paired pulse depression by changing the amplitude of the pulse voltage [42]. Zhou et al. prepared a superflexible protein paper substrate with good physical flexibility and excellent electrical properties, and, through a simple thermochemical reaction, they prepared an Au/EA/Au memristor, which still showed bipolar I-V characteristics in the bending state and type-switching behavior [43]. Sung et al. prepared Al/EA-GQD/ITO biomimetic synapse devices based on a hybrid nanocomposite of egg albumin (EA) and graphene quantum dots (GQDs). The I-V characteristics of the device exhibited clockwise hysteresis behavior under continuous positive and negative voltage scans [44]. Ghosh et al. used aloe vera flower extract as the active layer to create a biomemristor. Their device can achieve a high current-switching ratio and stable cyclability and exhibits two different extraction solutions in the preparation state and in the chemical reduction state [45]. Sun et al. embedded graphene into anthocyanins to make memristors and manipulated the I-V properties through the protonation of graphene to produce a self-selected memristor effect [41]. Saha et al. synthesized water-soluble sodium caseinate (NaCas), using the natural casein extracted from edible animal milk, and used it to prepare an Al/NaCas/ITO biomemristor. The device showed a large switching-current ratio, a long retention time, and a stable cycle durability [46]. It is worth studying the use of biological memristors to further realize artificial synapses and artificial neurons [47–50].

Polymethyl methacrylate (PMMA) easily forms a film due to its high transmittance and is often used as an insulating layer in organic thin-film transistors. Graphene quantum dots (GQDs), as a new type of quantum dot, have a good biocompatibility, a low cytotoxicity, and photoluminescence properties, making them very suitable as dopants for biological materials. In this paper, Al/PMMA/egg albumen (EA)-GQDs/PMMA/indium tin oxide (ITO) biomemristors were fabricated using the egg protein as a dielectric layer. The PMMA was added as an insulating layer on both sides of the EA dielectric layer, and the GQDs were doped to increase the light-sensitive properties of the device. The electrons in the GQDs were injected from the quantum dots into the dielectric layer or into the adjacent quantum dots under optical excitation; a pathway composed of GQDs was formed in the EA-GQDs dielectric layer, and electrons were transmitted on this pathway. The device successfully performed nine brain synaptic functions: excitatory postsynaptic current (EPSC), paired-pulse facilitation (PPF), short-term potentiation (STP), short-term depression (STD), the transition from short-term plasticity to long-term plasticity, spike-timing-dependent plasticity (STDP), spike-rate-dependent plasticity (SRDP), the process of learning, forgetting, and relearning, and Pavlov associative memory under UV light stimulation. The successful simulation of the synaptic behavior of this device provides the possibility for biomaterials to realize neuromorphic computing.

2. Materials and Methods

2.1. Device Fabrication

Fresh eggs were cut, and the egg white solution was extracted from them. We mixed 0.5 mL of EA and 5 mL of deionized water at a ratio of 1:10, placed it in an ultrasonic cleaner to disperse for 15 min, and mixed it thoroughly with 2.75 mL of 30% GQDs. The PMMA powder (400 mg) was mixed with 10 mL of anisole solution and stirred with a magnetic stirrer for 12 h. The glass with the ITO bottom electrode was ultrasonically cleaned with absolute ethanol and deionized water for 15 min each. The PMMA solution was dropped onto the ITO-conductive glass and spin-coated at 1000 rpm for 20 s, and the spin-coated PMMA substrate was placed in a drying oven at 100 °C for 1 h. The mixed solution of EA and GQDs was drop-coated onto the PMMA insulating layer and spin-coated at 4000 rpm for 40 s, and the spin-coated substrate was placed in a drying oven at 105 °C for 10 min. The PMMA solution was drop-coated onto the EA layer, spin-coated at 1000 rpm for 20 s, and then placed in a drying oven to cure for 1 h. A layer of Al electrodes was deposited onto the upper PMMA insulating layer using the vacuum evaporation method. Finally, the prepared device was placed in a vacuum-drying oven and dried at 105 °C for 10 min for annealing.

2.2. Instrument

The UV–Vis spectra of the SA materials were obtained with an ultraviolet–visible spectrophotometer (UV/VIS, TU-1901) (Beijing Purkinje General Instrument Co., Ltd., Beijing, China). The electrical characteristics of the prepared device were tested using a semiconductor parameter tester (Keithley 4200) (Keithley, Solon, OH, USA). During the electrical test of the device, the ITO bottom electrode was grounded, and a bias voltage was applied to the aluminum top electrode at the same time. The cross sections of the devices were characterized by scanning electron microscopy (Hitachi S-3400 N, Hitachi, Tokyo, Japan).

3. Results

The manufacturing flow chart of the Al/PMMA/EA–GQDs/PMMA/ITO device is shown in Figure 1a. The device's structure is Al/PMMA/EA–GQDs/PMMA/ITO, as shown in Figure 1b. The top electrode material is aluminum; the active layer is PMMA/EA–GQDs/PMMA, and the bottom electrode is ITO. The cross-section of the device is observed using a scanning electron microscope, as shown in Figure 1c, with PMMA (53 nm), EA (28 nm), PMMA (10 nm), and ITO (200 nm), in order from top to bottom. The optical analysis of the EA–GQD film using the UV–visible light spectrum is shown in Figure 1d. The wavelength corresponding to E_g is obtained through the intersection of the edge tangent line of the absorption peak and the correction baseline. The edge of the absorption peak of the EA–GQD film is located at a wavelength of $\lambda = 465$ nm, according to the following:

$$E_g = \frac{hc}{\lambda} \quad (1)$$

In Equation (2), E_g is the band gap width; $h = 6.62 \times 10^{-34}$ J·s is Planck's constant; $c = 3 \times 10^8$ m/s is the photon speed, and λ is the absorption wavelength. The bandgap of EA–GQDs is approximately 2.67 eV.

Figure 2a shows the electrical characteristics of the device. In the negative voltage scan of 0–5.00 V, when the set voltage (V_{set}) is -0.75 V, the device changes from a high resistance state (HRS) to a low resistance state (LRS), realizing the set process. In the positive voltage scan of 0–5.00 V, the device changes from the LRS to the HRS under the reset voltage (V_{reset}) of 3.20 V, completing the reset process. Figure 2b is a schematic diagram of the switching-current ratio of the device. The maximum on/off current ratio of the device is approximately 10^4 . The device can perform 100 cycles in the same cell, as shown in Figure 2c. The results show that the Al/PMMA/EA–GQDs/PMMA/ITO device has a stable resistance-switching memory behavior.

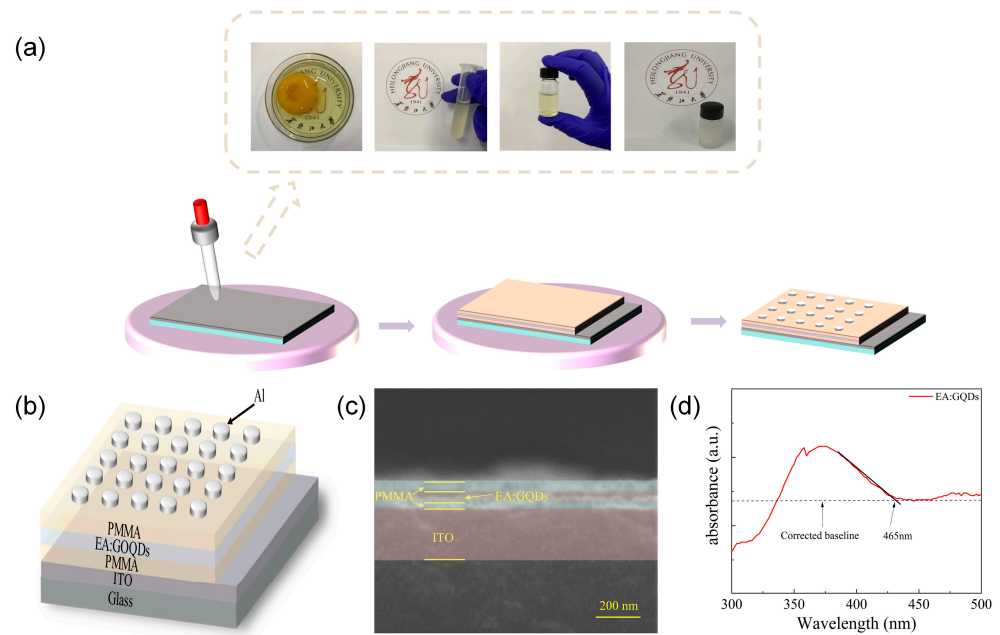


Figure 1. (a) Al/PMMA/EA-GQDs/PMMA/ITO's fabrication flow chart. (b) Schematic diagram of the structure of the device. (c) SEM photos of the cross-section of the device. (d) UV-Vis absorption spectra of the EA-GQD film.

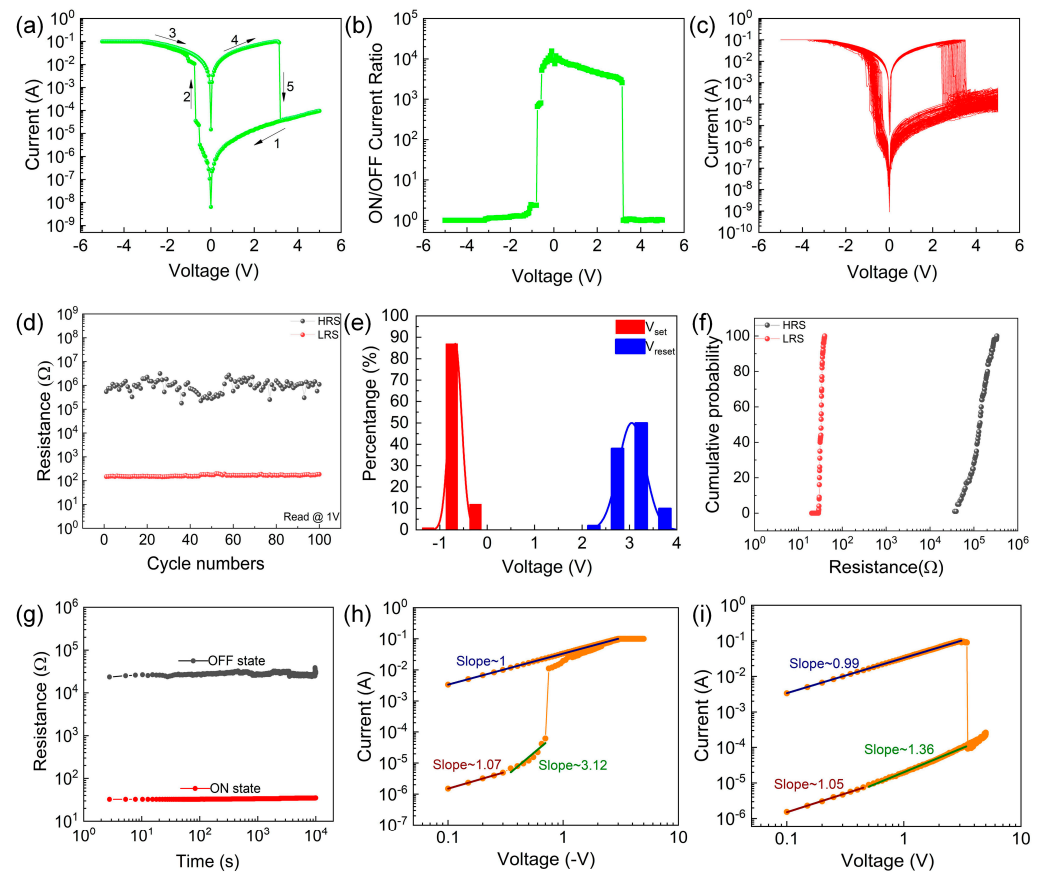


Figure 2. Electrical characteristics of the device. (a) Typical I-V characteristics. (b) ON/OFF current ratio. (c) 100-scan I-V characteristics. (d) Switching-endurance property. (e) Threshold voltage distribution histogram. (f) Resistance accumulation probability. (g) Retention property. (h) I-V characteristic curve under negative voltage. (i) I-V characteristic curve under a positive voltage.

The device proposed in the manuscript can complete 100 cycles, and Figure 2d shows the distribution of the high and low resistance states of the device under the limiting voltage of 1 V during the cycle. Figure 2e shows the threshold voltage distribution of the device. The average value of V_{set} for the Al/PMMA/EA-GQDs/PMMA/ITO device is -0.67 V, with a standard deviation of 0.13 V. The average value for the V_{reset} process is 3.05 V, with a standard deviation of 0.28 V. These results indicate that the device exhibits an excellent stability. Figure 2f shows the cumulative resistance probability of the Al/PMMA/EA-GQDs/PMMA/ITO device for 100 consecutive scans of the same cell at a voltage of 0.1 V. The median values of R_{HRS} and R_{LRS} are $1.85 \times 10^5 \Omega$ and 30.01Ω , respectively. The R_{LRS} distribution of the equipment is relatively concentrated, with a coefficient of variation of approximately 0.19, and the coefficient of variation of the RHRS of the device is 0.46, indicating the good consistency of the device. The retention time of the device was tested at 1 V, as shown in Figure 2g. The test results show that the device is maintained for more than 1×10^4 s in both the HRS and the LRS: the HRS remains at $2.75 \times 10^4 \Omega$, and the LRS remains at 34.37Ω . The fitting results of the I-V characteristic curve of the Al/PMMA/EA-GQDs/PMMA/ITO memristor under positive and negative voltages in double logarithmic coordinates are shown in Figure 2h,i. In Figure 2h, the slope of the fitted curve in the LRS is one, showing linearity, which is consistent with the ohmic conduction mechanism ($I \propto V$). The fitting curve of the HRS is divided into two parts, and the logarithmic curve of the HRS is a quadratic curve that shows a power relationship ($I \propto V^2$). In the low voltage region, the slope of the fitting curve is 1.07, which is consistent with the ohmic conduction mechanism. In the high voltage region, the slope of the fitting curve is 3.12, which is consistent with the space-charge-limited current effect. When the bias voltage reaches V_{SET} , the conductive filament connects the upper and lower electrodes, and the logarithmic I-V curve of the LRS becomes linear. The same is true for the positive voltage region, as shown in Figure 2i. Compared to the devices of undoped GQDs, the introduction of GQDs increases the number of defects in the dielectric layer so that more electrons injected into the dielectric layer are captured by the traps.

To simulate the excitatory postsynaptic current (EPSC) behavior of the Al/PMMA/EA-GQDs/PMMA/ITO artificial synapse, the bottom electrode ITO is connected to the ground to simulate the presynaptic membrane, and the top electrode Al is connected to the excitation voltage to simulate the postsynaptic membrane. As shown in Figure 3a, the current increased rapidly with the increasing excitation voltage; after the application of the excitation voltage was stopped, the current gradually decreased and, finally, stabilized. The EPSC current of the device increases with increasing negative excitation voltage under different levels of excitation stimulation, but its degree of increase decreases gradually. The higher the EPSC current, the longer it takes to drop to a stable value; in this scenario, the corresponding stable current is also higher, indicating the excellent nonvolatility of the device. As shown in Figure 3b, the device exhibits paired-pulse facilitation (PPF) behavior in response to an excitation stimulus. The response current for the first stimulus A_1 is 3.77×10^{-2} A, and the response current for the second stimulus A_2 is 7.17×10^{-2} A. The effect of this on the artificial synapse is expressed as the PPF exponent (A_2/A_1) for two stimuli with different time intervals (Δt). As shown in Figure 3c, the PPF index gradually decreases from 240% to 160% as the Δt between the two excitations increases. The excitation shown in Figure 3d is applied to the device to simulate the potentiation and depression behaviors. The artificial synapse exhibited an increase in conductance and a decrease in conductance during the potentiation and depression behaviors, respectively. In Figure 3e, the device potentiation and depression behaviors under ten consecutive excitation stimuli, showing that the device has a good synaptic plasticity.

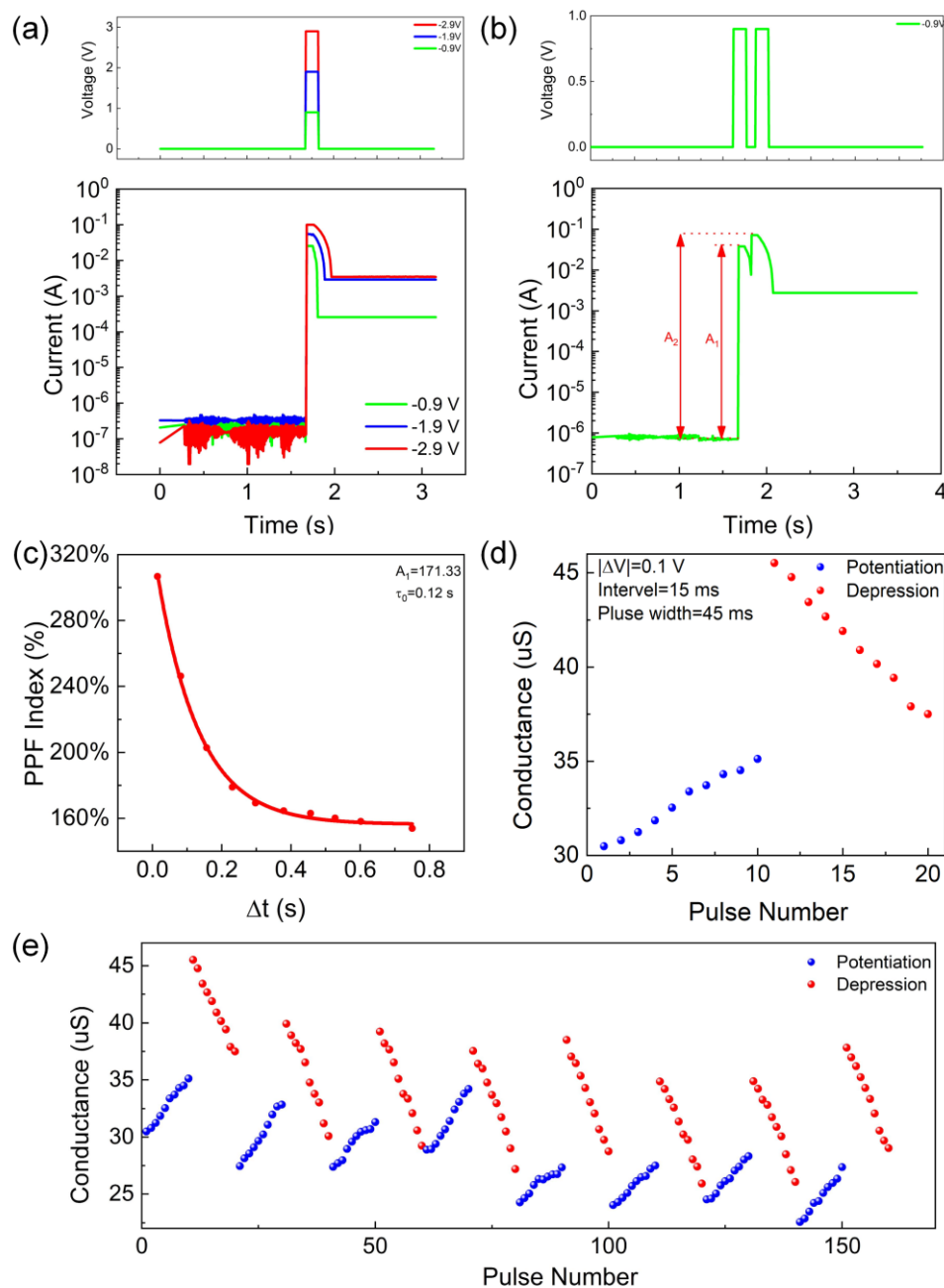


Figure 3. Short-term plasticity of the device: (a) EPSC behaviors corresponding to pulse wave-forms with different amplitudes. (b) PPF neurobehavior. (c) The PPF index (A_2/A_1) is affected by two consecutive presynaptic pulses, and Δt is the time between two presynaptic pulses. (d) Synaptic weight change $\Delta W(A_2 - A_1/A_1)$ affected by two consecutive presynaptic pulses. Potentiation and depression behaviors of the device. (e) Potentiation and depression behaviors under 100 consecutive pulses.

In the human brain, short-term memory can be transformed into long-term memory by repeated stimuli: this is one of the most important properties of humans' memory function. The transition from short-term plasticity (STP) to long-term plasticity (LTP) in the Al/PMMA/EA-GQDs/PMMA/ITO memristors was investigated. As the number of excitations increased, the decrease in synaptic weights gradually decreased, and the stable synaptic weights increased when the excitation was removed. In particular, the synaptic weight decreased the fastest when one excitation was applied and the least when eighty consecutive excitations were applied but, finally, returned to a stable state, as shown

in Figure 4a. In Figure 4b, the rising trend of the relative current change ($A_2 - A_1$) with increasing excitation frequency is gradually significant, demonstrating the good pulse-rate-dependent plasticity behavior of the device. At the same time, as the excitation rate increases, the synaptic weight increases more obviously, and the synaptic weight reaches its maximum when the excitation interval is $10 \mu\text{s}$. The pulse-time-dependent plasticity (STDP) observed in biological synapses is generally expressed with the following equation:

$$\Delta W = \begin{cases} A_+ e^{-|\Delta t|/\tau_+} + \Delta W_{0+}, & \Delta t > 0 \\ A_- e^{-|\Delta t|/\tau_-} + \Delta W_{0-}, & \Delta t < 0 \end{cases} \quad (2)$$

where A_+ and A_- represent the scaling factors; τ_+ and τ_- represent the time constants, and ΔW represents the synaptic weights. The STDP curve of the device fits well with Equation (2), and the relative change in synaptic weight (ΔW) decreases as $|\Delta t|$ increases, as shown in Figure 4c. To implement the learning experience, the AI/PMMA/EA-GQDs/PMMA/ITO synaptic device was used to simulate the learning, forgetting, and relearning process. First, it can be seen from Figure 4d that, after 50 consecutive excitation stimuli, the synaptic weight gradually increases with the increasing stimulation, which represents the learning behavior of the synapse. Then, after removing the stimulus, it is observed that the synaptic weights decay spontaneously with time and stabilize after a period of time, a process which represents the forgetting behavior of the synapses (Figure 4e). This is similar to the phenomenon where the information learned by a human brain is often partially forgotten after a period of time. Finally, after the spontaneous decay, 10 excitations were sufficient for the synaptic device to acquire the same level of weights as in Figure 4d (Figure 4f). The artificial synaptic device relearns previously forgotten information faster than the first time, a phenomenon similar to the relearning behavior in the brain.

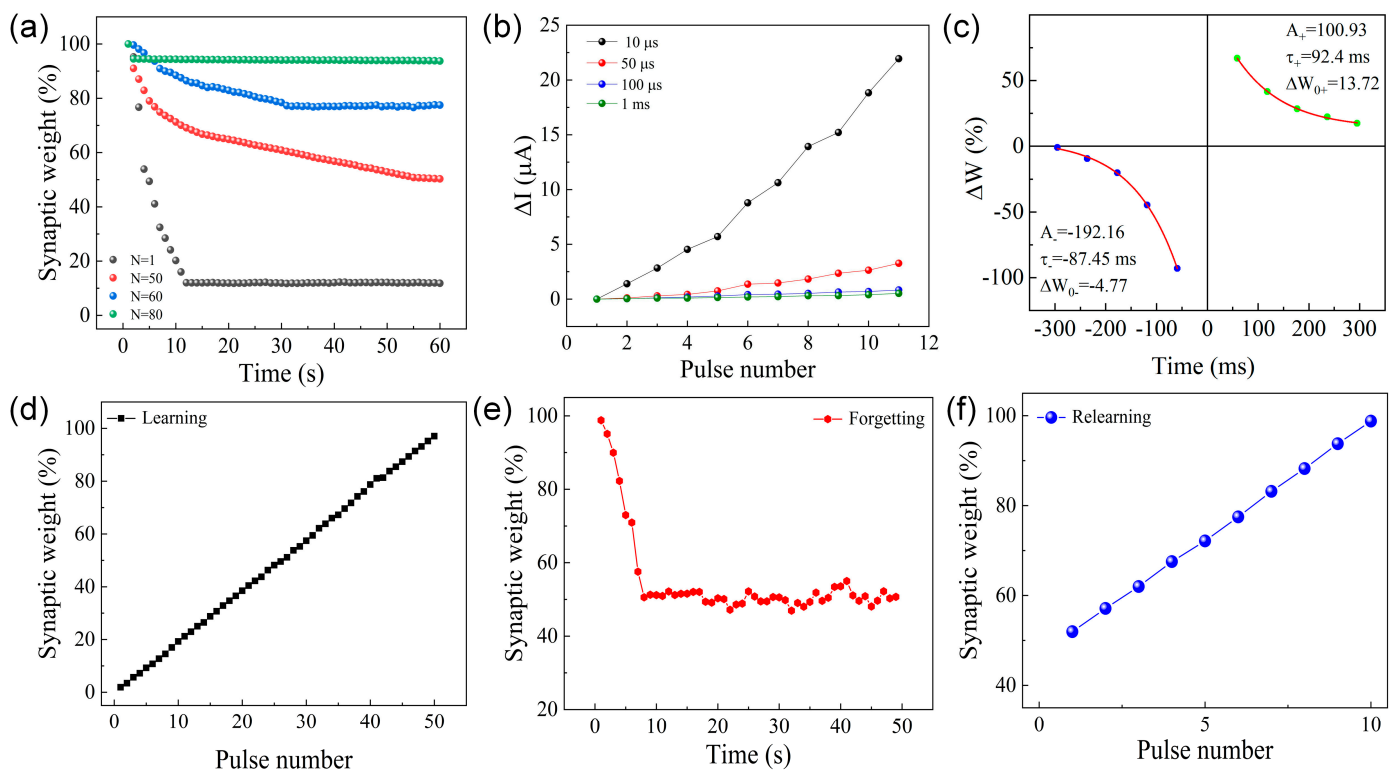


Figure 4. (a) Variation in synaptic weights with retention time after the application of different numbers of excitations. (b) Spike-rate-dependent plasticity. (c) Spike-time-dependent plasticity. (d) Learning behavior, (e) forgetting behavior, and (f) relearning behavior of human synapses.

When a negative voltage is applied to the Al electrode, the electrons tunnel directly into the EA–GQDs layer. As the voltage gradually increases, the energy band gradually bends so that a large potential barrier exists between the PMMA and EA–GQD layers, hindering the formation of internal conductive filaments. When the voltage increases to V_{set} , the trap state of the active layer is filled, and a conductive path is gradually formed, causing the resistance state of the device to suddenly change from a high resistance state (HRS) to a low resistance state (LRS). At this point, the electrons are allowed to travel freely in the device, and these electrons are continuously released from their trapped state. Therefore, the conduction mechanism of the LRS can be explained with ohmic conduction. When the trap states of the active layer are filled with the injected electrons, the device remains in the LRS even when gradually decreasing negative voltages are applied. In contrast, when a positive voltage is applied to the Al electrode, the electrons in the dielectric layer are continuously released from the trap center. When the voltage increases to V_{reset} , the conductive path is destroyed, causing the device to switch from the LRS to the HRS.

A UV light with a wavelength of 395 nm and a power of 171.42 mW/cm² was applied to the Al/PMMA/EA–GQDs/PMMA/ITO memristor. Figure 5 shows the conduction mechanism of the device under UV irradiation. When a negative voltage is applied to the Al electrode, since the PMMA layer is an insulating layer, a large number of positive and negative charges accumulate on both sides, and a top-to-bottom electric field is generated in the EA dielectric layer. Under ultraviolet irradiation, the electrons in GQDs may be injected from the quantum dots into the dielectric layer or into the adjacent quantum dots under photoexcitation. When the concentration of doped quantum dots is high, a pathway composed of GQDs is formed in the EA–GQD dielectric layer, and electrons are transported along this pathway under optical excitation. The generation of vias provides more electron transport paths, enhances the charge-injection efficiency, and, thus, increases the conductivity of the dielectric layer. The different electrical properties of the Al/PMMA/EA–GQDs/PMMA/ITO memristor with or without UV irradiation were analyzed. In this analysis, the pulsed electrical signal was used as a bell signal, and the ultraviolet irradiation was used as a food signal. The electrical properties of the device under these two signals was used as a stimulus response to realize Pavlovian associative memory.

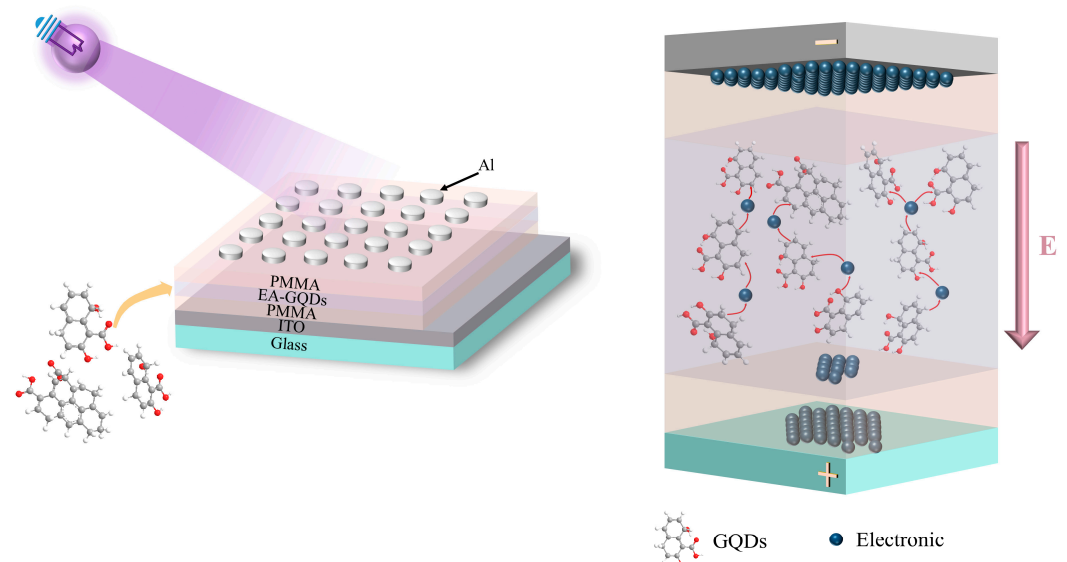


Figure 5. Conduction mechanism of the Al/PMMA/EA–GQDs/PMMA/ITO device under UV irradiation.

Applying voltage to the Al/PMMA/EA–GQDS/PMMA/ITO memristor is a ringtone stimulus, and applying UV irradiation to the memristor is a food stimulus, as shown in Figure 6. In the figure, W_0 is 1×10^{-4} A. When the synaptic weight is greater than W_0 ,

the dog secretes saliva, and, when the synaptic weight is less than W_0 , the dog does not secrete saliva. When the ringtone stimulus was applied, the current of the device was 2×10^{-5} A; the synaptic weight was less than the weight W_0 of salivation, and the dog did not salivate. When the food stimulus was applied, the current of the device was 3×10^{-4} A; the weight was greater than the weight W_0 of salivation, and the dog would salivate. The Al/PMMA/EA-GQDs/PMMA/ITO memristor realizes Pavlovian associative memory under the continuous action of pulsed voltage stimulation and UV irradiation stimulation. Figure 6 is divided into six stages. Stage 1 consists of the bell stimulus; the synaptic weight is smaller than the salivation weight W_0 ; the dog does not secrete saliva. Stage 2 covers the food stimulus; the synaptic weight is greater than the saliva secretion weight W_0 ; the dog secretes saliva. Stage 4 comprises food. The stimulation of the food and the bell stimulation work together, and the dog secretes saliva. In stage 5, after the food stimulation and bell stimulation, the dog is immediately stimulated by the bell. At this time, the synaptic weight decreases, but it is still greater than the salivation weight W_0 , and the dog secretes saliva. This process corresponds to the associative memory stage. If the dog continues to be stimulated by the bell, the synaptic weight will continue to decrease, which will lead to it weighting less than the weight of the saliva secretion W_0 . In this case, the dog would not secrete saliva, meaning that this process corresponds to the forgetting stage.

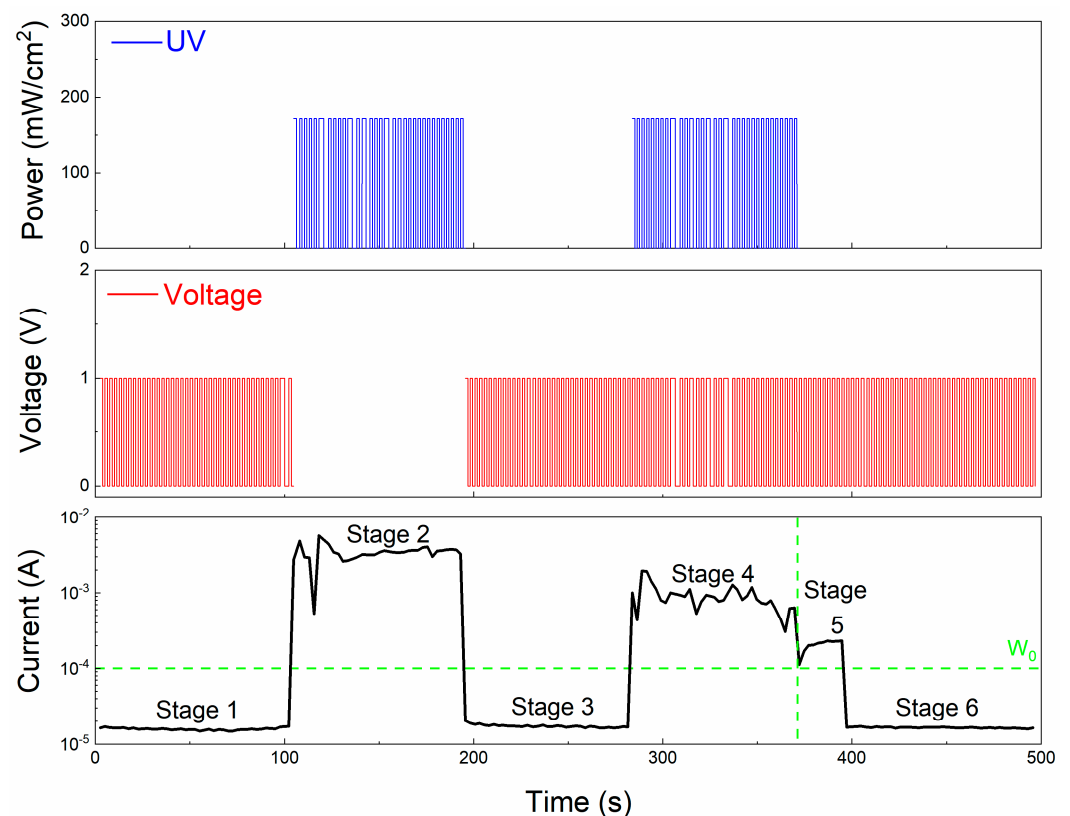


Figure 6. Pavlovian associative memory of the Al/PMMA/EA-GQDs/PMMA/ITO device under UV irradiation and pulsed stimulation.

4. Conclusions

In this paper, Al/PMMA/EA-GQDs/PMMA/ITO biomemristors were fabricated using egg protein as a dielectric layer. The PMMA was added to the upper and lower sides of the EA dielectric layer as an insulating layer, and the GQDs were doped in the EA resistive layer to increase the light-sensitive properties of the device. The electrons in the GQDs were injected from the quantum dots into the dielectric layer or into the adjacent quantum dots under the excitation of light. The EA-GQDs dielectric layer formed a pathway composed of GQDs, and electrons were transported on this pathway. After

testing, it could be seen that the device has good electrical characteristics. The device successfully simulates the following synaptic functions: EPSC, PPF, STP, STD, the transformation of short-term plasticity to long-term plasticity, STDP, SRDP, the process of learning, forgetting, and relearning, and Pavlov associative memory under UV light stimulation. The results show that the Al/PMMA/EA-GQDs/PMMA/ITO memristor has a strong potential for simulating biological synapses, which is of great significance to the development of neuromorphic computing systems.

Author Contributions: Data curation, S.W., J.X., Y.J. and T.Y.; Funding acquisition, L.W.; Investigation, L.W., S.W., J.X., Y.J., T.Y. and D.W.; Methodology, L.W.; Visualization, S.W.; Writing—original draft, L.W., S.W., J.X., Y.J. and T.Y.; Writing—review & editing, L.W. All authors have read and agreed to the published version of the manuscript.

Funding: This work was supported by the National Natural Science Foundation of China (Grant No. 62371183), the Heilongjiang Provincial Natural Science Foundation of China (Grant No. LH2021F045), and the Basic Research Project funded by the Basic Research Business Funding for Provincial Universities in the Heilongjiang Province (Grant No. 2022-KYYWF-1088).

Data Availability Statement: The data sets used and/or analyzed during the current study are available from the corresponding author upon reasonable request.

Conflicts of Interest: The authors declare no conflict of interest.

References

1. Merolla, P.A.; Arthur, J.V.; Alvarez-Icaza, R.; Cassidy, A.S.; Sawada, J.; Akopyan, F.; Jackson, B.L.; Imam, N.; Guo, C.; Nakamura, Y.; et al. Artificial brains. A million spiking-neuron integrated circuit with a scalable communication network and interface. *Science* **2014**, *345*, 668–673. [[CrossRef](#)] [[PubMed](#)]
2. Sheridan, P.M.; Cai, F.; Du, C.; Ma, W.; Zhang, Z.; Lu, W.D. Sparse coding with memristor networks. *Nat. Nanotechnol.* **2017**, *12*, 784–789. [[CrossRef](#)] [[PubMed](#)]
3. Jeong, D.S.; Kim, K.M.; Kim, S.; Choi, B.J.; Hwang, C.S. Memristors for Energy-Efficient New Computing Paradigms. *Adv. Electron. Mater.* **2016**, *2*, 1600090. [[CrossRef](#)]
4. Jo, S.H.; Chang, T.; Ebong, I.; Bhadviya, B.B.; Mazumder, P.; Lu, W. Nanoscale memristor device as synapse in neuromorphic systems. *Nano Lett.* **2010**, *10*, 1297–1301. [[CrossRef](#)] [[PubMed](#)]
5. Zhao, C.; Cheung, C.F.; Xu, P. High-efficiency submicroscale uncertainty measurement method using pattern recognition. *ISA Trans.* **2020**, *101*, 503–514. [[CrossRef](#)] [[PubMed](#)]
6. Yu, S.; Wu, Y.; Jeyasingh, R.; Kuzum, D.; Wong, H.S.P. An Electronic Synapse Device Based on Metal Oxide Resistive Switching Memory for Neuromorphic Computation. *IEEE Trans. Electron Devices* **2011**, *58*, 2729–2737. [[CrossRef](#)]
7. Wang, Z.; Yin, M.; Zhang, T.; Cai, Y.; Wang, Y.; Yang, Y.; Huang, R. Engineering incremental resistive switching in TaO_x based memristors for brain-inspired computing. *Nanoscale* **2016**, *8*, 14015–14022. [[CrossRef](#)]
8. Prezioso, M.; Merrih-Bayat, F.; Hoskins, B.D.; Adam, G.C.; Likharev, K.K.; Strukov, D.B. Training and operation of an integrated neuromorphic network based on metal-oxide memristors. *Nature* **2015**, *521*, 61–64. [[CrossRef](#)]
9. Yang, J.J.; Strukov, D.B.; Stewart, D.R. Memristive devices for computing. *Nat. Nanotechnol.* **2013**, *8*, 13–24. [[CrossRef](#)]
10. Pan, F.; Gao, S.; Chen, C.; Song, C.; Zeng, F. Recent progress in resistive random access memories: Materials, switching mechanisms, and performance. *Mater. Sci. Eng. R Rep.* **2014**, *83*, 1–59. [[CrossRef](#)]
11. Rajendran, B.; Liu, Y.; Seo, J.-s.; Gopalakrishnan, K.; Chang, L.; Friedman, D.J.; Ritter, M.B. Specifications of Nanoscale Devices and Circuits for Neuromorphic Computational Systems. *IEEE Trans. Electron Devices* **2013**, *60*, 246–253. [[CrossRef](#)]
12. Park, Y.; Lee, J.S. Artificial Synapses with Short- and Long-Term Memory for Spiking Neural Networks Based on Renewable Materials. *ACS Nano* **2017**, *11*, 8962–8969. [[CrossRef](#)] [[PubMed](#)]
13. Li, S.; Zeng, F.; Chen, C.; Liu, H.; Tang, G.; Gao, S.; Song, C.; Lin, Y.; Pan, F.; Guo, D. Synaptic plasticity and learning behaviors mimicked through Ag interface movement in an Ag/conducting polymer/Ta memristive system. *J. Mater. Chem. C* **2013**, *1*, 5292–5298. [[CrossRef](#)]
14. Hu, S.G.; Liu, Y.; Chen, T.P.; Liu, Z.; Yu, Q.; Deng, L.J.; Yin, Y.; Hosaka, S. Emulating the Ebbinghaus forgetting curve of the human brain with a NiO-based memristor. *Appl. Phys. Lett.* **2013**, *103*, 133701. [[CrossRef](#)]
15. Li, J.; Duan, Q.; Zhang, T.; Yin, M.; Sun, X.; Cai, Y.; Li, L.; Yang, Y.; Huang, R. Tuning analog resistive switching and plasticity in bilayer transition metal oxide based memristive synapses. *RSC Adv.* **2017**, *7*, 43132–43140. [[CrossRef](#)]
16. Lai, Q.; Zhang, L.; Li, Z.; Stickle, W.F.; Williams, R.S.; Chen, Y. Ionic/electronic hybrid materials integrated in a synaptic transistor with signal processing and learning functions. *Adv. Mater.* **2010**, *22*, 2448–2453. [[CrossRef](#)]
17. Kuzum, D.; Jeyasingh, R.G.; Lee, B.; Wong, H.S. Nanoelectronic programmable synapses based on phase change materials for brain-inspired computing. *Nano Lett.* **2012**, *12*, 2179–2186. [[CrossRef](#)]

18. Merolla/Yan, X.; Zhou, Z.; Ding, B.; Zhao, J.; Zhang, Y. Superior resistive switching memory and biological synapse properties based on a simple TiN/SiO₂/p-Si tunneling junction structure. *J. Mater. Chem. C* **2017**, *5*, 2259–2267.
19. Wang, Z.Q.; Xu, H.Y.; Li, X.H.; Yu, H.; Liu, Y.C.; Zhu, X.J. Synaptic Learning and Memory Functions Achieved Using Oxygen Ion Migration/Diffusion in an Amorphous InGaZnO Memristor. *Adv. Funct. Mater.* **2012**, *22*, 2759–2765. [[CrossRef](#)]
20. Kim, S.; Kim, H.; Hwang, S.; Kim, M.H.; Chang, Y.F.; Park, B.G. Analog Synaptic Behavior of a Silicon Nitride Memristor. *ACS Appl. Mater. Interfaces* **2017**, *9*, 40420–40427. [[CrossRef](#)]
21. Aziz, J.; Khan, M.F.; Neumaier, D.; Ahmad, M.; Kim, H.; Rehman, S.; Elahi, E.; Chavan, V.D.; Ghafoor, F.; Kadam, K.D.; et al. Improved memory performance of ALD grown HfO₂ films by nitrogen doping. *Mater. Sci. Eng. B* **2023**, *297*, 116755. [[CrossRef](#)]
22. Zhao, Y.Y.; Sun, W.J.; Wang, J.; He, J.H.; Li, H.; Xu, Q.F.; Li, N.J.; Chen, D.Y.; Lu, J.M. All-Inorganic Ionic Polymer-Based Memristor for High-Performance and Flexible Artificial Synapse. *Adv. Funct. Mater.* **2020**, *30*, 2004245. [[CrossRef](#)]
23. Ren, C.; Zhong, G.; Xiao, Q.; Tan, C.; Feng, M.; Zhong, X.; An, F.; Wang, J.; Zi, M.; Tang, M.; et al. Highly Robust Flexible Ferroelectric Field Effect Transistors Operable at High Temperature with Low-Power Consumption. *Adv. Funct. Mater.* **2019**, *30*, 2070005. [[CrossRef](#)]
24. Zhang, J.J.; Sun, H.J.; Li, Y.; Wang, Q.; Xu, X.H.; Miao, X.S. AgInSbTe memristor with gradual resistance tuning. *Appl. Phys. Lett.* **2013**, *102*, 183513. [[CrossRef](#)]
25. Gupta, V.; Lucarelli, G.; Castro-Hermosa, S.; Brown, T.; Ottavi, M. Investigation of hysteresis in hole transport layer free metal halide perovskites cells under dark conditions. *Nanotechnology* **2020**, *31*, 445201. [[CrossRef](#)] [[PubMed](#)]
26. Das, U.; Sarkar, P.; Paul, B.; Roy, A. Halide perovskite two-terminal analog memristor capable of photoactivated synaptic weight modulation for neuromorphic computing. *Appl. Phys. Lett.* **2021**, *118*, 182103. [[CrossRef](#)]
27. Gogoi, H.J.; Bajpai, K.; Mallajosyula, A.T.; Solanki, A. Advances in Flexible Memristors with Hybrid Perovskites. *J. Phys. Chem. Lett.* **2021**, *12*, 8798–8825. [[CrossRef](#)]
28. Wang, Y.; Liu, H.; Liu, P.; Lu, W.; Cui, J.; Chen, X.; Lu, M. Energy-efficient synaptic devices based on planar structured h-BN memristor. *J. Alloys Compd.* **2022**, *909*, 164775. [[CrossRef](#)]
29. Rehman, S.; Khan, M.F.; Rahmani, M.K.; Kim, H.; Patil, H.; Khan, S.A.; Kang, M.H.; Kim, D.-K. Neuro-transistor based on uv-treated charge trapping in mote2 for artificial synaptic features. *Nanomaterials* **2020**, *10*, 2326. [[CrossRef](#)]
30. Song, Y.-W.; Song, M.-K.; Choi, D.; Kwon, J.-Y. Encapsulation-enhanced switching stability of MoS₂ memristors. *J. Alloys Compd.* **2021**, *885*, 161016. [[CrossRef](#)]
31. Hwang, S.W.; Tao, H.; Kim, D.H.; Cheng, H.; Song, J.K.; Rill, E.; Brenckle, M.A.; Panilaitis, B.; Won, S.M.; Kim, Y.S.; et al. A physically transient form of silicon electronics. *Science* **2012**, *337*, 1640–1644. [[CrossRef](#)] [[PubMed](#)]
32. Dagdeviren, C.; Hwang, S.W.; Su, Y.; Kim, S.; Cheng, H.; Gur, O.; Haney, R.; Omenetto, F.G.; Huang, Y.; Rogers, J.A. Transient, biocompatible electronics and energy harvesters based on ZnO. *Small* **2013**, *9*, 3398–3404. [[CrossRef](#)] [[PubMed](#)]
33. Hwang, S.-W.; Kim, D.-H.; Tao, H.; Kim, T.-i.; Kim, S.; Yu, K.J.; Panilaitis, B.; Jeong, J.-W.; Song, J.-K.; Omenetto, F.G.; et al. Materials and Fabrication Processes for Transient and Bioresorbable High-Performance Electronics. *Adv. Funct. Mater.* **2013**, *23*, 4087–4093. [[CrossRef](#)]
34. Ji, Y.; Cho, B.; Song, S.; Kim, T.W.; Choe, M.; Kahng, Y.H.; Lee, T. Stable switching characteristics of organic nonvolatile memory on a bent flexible substrate. *Adv. Mater.* **2010**, *22*, 3071–3075. [[CrossRef](#)] [[PubMed](#)]
35. Liu, G.; Wang, C.; Zhang, W.; Pan, L.; Zhang, C.; Yang, X.; Fan, F.; Chen, Y.; Li, R.-W. Organic Biomimicking Memristor for Information Storage and Processing Applications. *Adv. Electron. Mater.* **2016**, *2*, 1500298. [[CrossRef](#)]
36. Chung, T.H.; Dhar, B.R. Paper-based platforms for microbial electrochemical cell-based biosensors: A review. *Biosens. Bioelectron.* **2021**, *192*, 113485. [[CrossRef](#)]
37. Chang, J.W.; Wang, C.G.; Huang, C.Y.; Tsai, T.D.; Guo, T.F.; Wen, T.C. Chicken albumen dielectrics in organic field-effect transistors. *Adv. Mater.* **2011**, *23*, 4077–4081. [[CrossRef](#)]
38. Wu, W.; Han, S.T.; Venkatesh, S.; Sun, Q.; Peng, H.; Zhou, Y.; Yeung, C.; Li, R.K.Y.; Roy, V.A.L. Biodegradable skin-inspired nonvolatile resistive switching memory based on gold nanoparticles embedded alkali lignin. *Org. Electron.* **2018**, *59*, 382–388. [[CrossRef](#)]
39. Sun, B.; Zhang, X.; Zhou, G.; Li, P.; Zhang, Y.; Wang, H.; Xia, Y.; Zhao, Y. An organic nonvolatile resistive switching memory device fabricated with natural pectin from fruit peel. *Org. Electron.* **2017**, *42*, 181–186. [[CrossRef](#)]
40. Yu, F.; Zhu, L.Q.; Gao, W.T.; Fu, Y.M.; Xiao, H.; Tao, J.; Zhou, J.M. Chitosan-based polysaccharide-gated flexible indium tin oxide synaptic transistor with learning abilities. *ACS Appl. Mater. Interfaces* **2018**, *10*, 16881–16886. [[CrossRef](#)]
41. Sun, B.; Guo, T.; Zhou, G.; Wu, J.; Chen, Y.; Zhou, Y.N.; Wu, Y.A. A battery-like self-selecting biomemristor from earth-abundant natural biomaterials. *ACS Appl. Bio Mater.* **2021**, *4*, 1976–1985. [[CrossRef](#)] [[PubMed](#)]
42. Yan, X.; Li, X.; Zhou, Z.; Zhao, J.; Wang, H.; Wang, J.; Zhang, L.; Ren, D.; Zhang, X.; Chen, J.; et al. Flexible transparent organic artificial synapse based on the tungsten/egg albumen/indium tin oxide/polyethylene terephthalate memristor. *ACS Appl. Mater. Interfaces* **2019**, *11*, 18654–18661. [[CrossRef](#)]
43. Zhou, G.; Ren, Z.; Wang, L.; Sun, B.; Duan, S.; Song, Q. Artificial and wearable albumen protein memristor arrays with integrated memory logic gate functionality. *Mater. Horiz.* **2019**, *6*, 1877–1882. [[CrossRef](#)]
44. Sung, S.; Park, J.H.; Wu, C.; Kim, T.W. Biosynaptic devices based on chicken egg albumen: Graphene quantum dot nanocomposites. *Sci. Rep.* **2020**, *10*, 1255. [[CrossRef](#)] [[PubMed](#)]

45. Ghosh, T.; Kandpal, S.; Pathak, D.K.; Tanwar, M.; Rani, C.; Chaudhary, A.; Kumar, R. Aloe vera flower extract as a botanical resistive memory element: A natural memristor! *ACS Appl. Electron. Mater.* **2021**, *3*, 1556–1559. [[CrossRef](#)]
46. Saha, M.; Nawaz, S.M.; Keshari, B.K.; Mallik, A. Natural-casein-based biomemristor with pinched current–voltage characteristics. *ACS Appl. Bio Mater.* **2022**, *5*, 833–840. [[CrossRef](#)]
47. Wang, L.; Zhang, Y.; Zhang, P.; Wen, D. Flexible Transient Resistive Memory Based on Biodegradable Composites. *Nanomaterials* **2022**, *12*, 3531. [[CrossRef](#)]
48. Wang, L.; Yang, T.; Wen, D. Tunable multilevel data storage bioresistive random access memory device based on egg albumen and carbon nanotubes. *Nanomaterials* **2021**, *11*, 2085. [[CrossRef](#)]
49. Wang, L.; Zhu, H.; Wen, D. Bioresistive random-access memory with gold nanoparticles that generate the coulomb blocking effect can realize multilevel data storage and synapse simulation. *J. Phys. Chem. Lett.* **2021**, *12*, 8956–8962. [[CrossRef](#)]
50. Wang, L.; Wei, S.; Xie, J.; Wen, D. Bioartificial Synapses for Neuromorphic Computing. *ACS Sustain. Chem. Eng.* **2023**, *11*, 2229–2237. [[CrossRef](#)]

Disclaimer/Publisher’s Note: The statements, opinions and data contained in all publications are solely those of the individual author(s) and contributor(s) and not of MDPI and/or the editor(s). MDPI and/or the editor(s) disclaim responsibility for any injury to people or property resulting from any ideas, methods, instructions or products referred to in the content.